J. Fluid Mech. (2009), *vol.* 636, *pp.* 397–425.
doi:10.1017/S0022112009007952

Low-frequency dynamics of shock-induced separation in a compression ramp interaction

B. GANAPATHISUBRAMANI[1]†, N. T. CLEMENS[2] AND D. S. DOLLING[2]

[1]Department of Aeronautics, Imperial College London, Prince Consort Road, London SW7 2AZ, UK

[2]Centre for Aeromechanics Research, The University of Texas at Austin, 210 E. 24th Street, WRW220, Mail Code C0604, Austin TX 78712, USA

(Received 13 December 2007 and in revised form 1 May 2009)

The low-frequency dynamics of the shock-induced separation region in a Mach 2 compression ramp interaction is investigated by performing high-speed particle image velocimetry (HSPIV) measurements, at a rate of 6 kHz, in a streamwise–spanwise plane. The HSPIV measurements made in the upstream turbulent boundary layer indicate the presence of spanwise strips of elongated regions of uniform streamwise velocity that extend to lengths greater than 30δ, validating previous results based on planar laser scattering measurements obtained by Ganapathisubramani, Clemens & Dolling (*J. Fluid Mech.*, vol. 585, 2007, p. 369). At a wall normal-location of $y/\delta = 0.2$, a surrogate for separation based on a velocity threshold is found to fluctuate over a streamwise range of $\pm 1.2\delta$, consistent with previous studies. The amplitude of unsteadiness has contributions from at least two sources that are related to the incoming boundary layer. First, the velocity threshold based surrogate separation line exhibits large-scale undulations along the spanwise direction that conform to the passage of elongated low- and high-speed regions in the upstream boundary layer. This motion is classified as the *local influence* of the upstream boundary layer. Second, the spanwise-averaged surrogate separation is found to respond to the overall change in streamwise velocity in the incoming boundary layer and is classified as the *global influence* of the upstream boundary layer. However, this *global influence* includes the contributions from the elongated low- and high-speed regions. Preliminary findings based on statistical analysis suggest that the local influence contributes nearly 50 % more than the global influence. Regardless, the low-frequency unsteadiness of the separation-region can be attributed to the *local* and *global* influences of the incoming boundary layer.

1. Introduction

Shock-wave/boundary layer interactions (SBLI) has been an area of extensive research for over 50 years (Dolling 2001). One of main open issues in this topic is the frequency range that characterizes the unsteadiness of shock-induced separation region. Previous studies have found that the frequency of unsteadiness of shock-induced separation is at least an order of magnitude lower than the nominal boundary layer frequency based on free stream velocity and boundary

† Email address for correspondence: g.bharath@imperial.ac.uk

layer thickness (see Dolling 2001 among others). The characteristic time scale of the incoming boundary layer is of order δ/U_∞ (where U_∞ is the free stream velocity and δ is the 99 % boundary layer thickness of the incoming boundary layer), while the time scale of the low-frequency unsteadiness is of order $10\delta/U_\infty$–$100\delta/U_\infty$. The causes that may be responsible for this order of magnitude discrepancy remain unresolved.

There are at least two possible sources that influence the low-frequency unsteadiness of the shock-induced separation region, (i) upstream influence: the structures in the incoming boundary layer and (ii) downstream influence: characteristic time and length scales of the separation bubble. Some researchers have indicated that a downstream influence is a more likely cause for the low-frequency unsteadiness. Dussauge, Dupont & Debieve (2006) performed experimental investigations (pressure measurements and particle image velocimetry (PIV)) in a reflected shock/boundary layer interaction and concluded that the three-dimensional structure of the separation bubble may be at the origin of the low-frequency unsteadiness. Dupont, Haddad & Debieve (2006) evaluated characteristic time and length scales of the shock motion and the downstream interaction for various reflected shock interactions and found strong statistical link between the low-frequency shock motion and the low-frequency events inside the separated zone. However, the exact cause for the low-frequency events in the separated zone is not known.

Alternately, other researchers have indicated the presence of an upstream influence. Beresh, Clemens & Dolling (2002) at Mach 5 and Hou, Clemens & Dolling (2003) at Mach 2 showed that the motion of the shock foot responds to velocity fluctuations in the upstream boundary layer. It was found that the shock foot moves upstream (downstream) if the lower part of the upstream boundary layer is slower (faster). Consequently, the separation region extends farther upstream (the scale is larger) if the upstream boundary layer is slower and the separation region is smaller if the boundary layer is faster. Although this provides a physical representation for the motion of the separation region, the exact mechanism involved is still unclear.

Despite the contrast, one aspect that is common to both viewpoints is the fact that the physical mechanism that causes the low-frequency unsteadiness remains unknown. Recently, Ganapathisubramani, Clemens & Dolling (2006) performed PIV measurements in streamwise–spanwise planes of a supersonic boundary layer and identified the presence of long low- and high-speed regions that extended to lengths greater than 8δ. Subsequently, Ganapathisubramani, Clemens & Dolling (2007) established a relationship between the presence of these long low- and high-speed regions and the upstream envelope of shock-induced separation region. Using evidence based on correlations and conditional averages, they proposed a physical model where the upstream envelope of the separation region responds to the passage of these elongated uniform low- and high-speed regions. The dynamics of this proposed model is not clear since the conclusions were based on instantaneous velocity data without any temporal information.

The aim of the current work is to further enhance the understanding of the role of upstream turbulent boundary layer fluctuations on shock-wave/boundary layer interactions. We follow the work performed by Ganapathisubramani *et al.* (2007) and aim to investigate the role of upstream boundary layer velocity fluctuations on the low-frequency dynamics of the separated region in a Mach 2 compression ramp interaction by performing high-speed particle image velocimetry (HSPIV) in streamwise–spanwise planes.

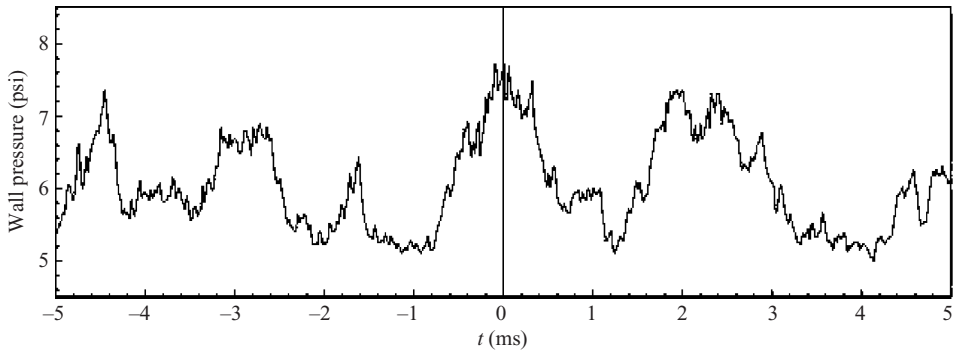

FIGURE 1. Wall-pressure time history in the intermittent region of the compression ramp interaction. Figure reproduced from Hou (2003).

2. Experimental facility and details

2.1. *Wind tunnel facility*

All of the experiments were conducted in the Mach 2 blowdown tunnel of the University of Texas at Austin. The stagnation chamber pressure and temperature for the present experiments were approximately 261 ± 7 kPa and 292 ± 5 K, respectively. The free stream conditions were as follows: Mach number $M_\infty = 2$ and velocity $U_\infty = 510\,\mathrm{ms}^{-1}$and turbulence intensity of less than 1 %. The incoming turbulent boundary layer underwent natural transition and developed on the wind tunnel floor under approximately adiabatic wall temperature conditions. Preliminary PIV measurements were performed in the streamwise-wall-normal planes to characterize the upstream boundary layer (see Ganapathisubramani 2007 for details). The wall-normal profile of the mean streamwise velocity obtained from these measurements was used to compute various boundary layer parameters. The boundary layer thickness δ (99 % of U_∞) is 12.5 mm, the incompressible momentum thickness (θ) is 1 mm and the incompressible displacement thickness (δ^*) is 1.6 mm. The shape factor of the boundary layer $\mathrm{H} = \delta^*/\theta = 1.6$ is consistent with the values obtained in various other studies in the literature (see Smits & Dussauge 1996). The skin friction velocity u_τ is $18.5\,\mathrm{ms}^{-1}$and the Reynolds number based on momentum thickness and free stream conditions $Re_\theta = \rho_\infty U_\infty \theta/\mu_\infty$ of 38 000.

The shock-wave/boundary layer interaction was generated using a 20° compression ramp that spanned the entire width of tunnel. Hou (2003) performed detailed wall-pressure measurements by using an array of fast response pressure transducers to qualify the nature of unsteadiness in this interaction. Figure 1 shows the wall-pressure history in the intermittent region of the interaction. These pressure measurements were obtained using Kulite fast response pressure transducers (Model XCQ-062-50A) at a streamwise location of $x = -3\delta$, upstream of the ramp foot. The figure indicates the presence of large-scale low-frequency oscillations in pressure that occur over a time period of 1–3 ms. A small-scale jitter is superimposed on these large-scale fluctuations. The large-scale unsteadiness corresponds to a non-dimensional frequency ($f\delta/U_\infty$) in the range 0.008–0.025. It is the origin of this low-frequency unsteadiness that remains elusive. The goal of the current work is to perform HSPIV measurements to understand the role of incoming boundary layer and its contribution to this low-frequency unsteadiness. HSPIV measurements are performed at a sampling frequency (f_s) of 6 kHz, which corresponds to a non-dimensional frequency ($f_s\delta/U_\infty$) of 0.15 that is at least 6 times higher than the frequency of interest. Previous PIV measurements at

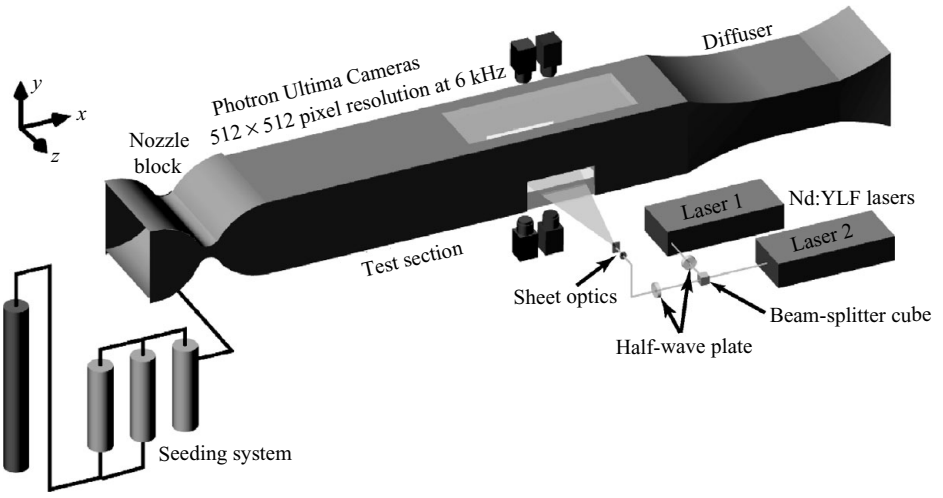

FIGURE 2. Experimental setup.

low frequencies (about 10 Hz) provided randomly sampled data that can be used for statistical analysis. The HSPIV measurements reported in this paper enable analysis of time sequences and computation of temporal correlations that can capture the low-frequency unsteadiness. It must be noted that the acquisition rate of HSPIV is not sufficient to capture the higher temporal frequencies that are also present in the unsteadiness and in the upstream boundary layer.

2.2. *High-Speed Particle Image Velocimetry*

The HSPIV system used in the current study is similar to the one used by Bueno *et al.* (2005) in which a shock-wave/boundary layer interaction was investigated in a streamwise-wall-normal plane. A schematic illustration of the experimental setup is shown in figure 2. The two laser pulses required for PIV are produced by two diode-pumped Nd:YLF lasers (wavelength 527 nm, Coherent Evolution-90). Each laser can output an average power of 90 W at 10 kHz and 527 nm. In the current study, a repetition rate of 6 kHz was used. At this frequency the output power was 75W per laser head, which corresponds to approximately 12.5 mJ pulse^{-1}.

The individual laser beams were combined to have a common optical path by means of a polarizing beam splitter. Laser 1 was passed through a half-wave plate to rotate its polarization from horizontal to vertical, and then combined with laser 2 by using a polarizing beam splitter cube as shown in figure 2. The combined laser beams were passed through another half-wave plate to rotate their polarization by 45° such that the polarization vectors would have approximately the same orientation with respect to the scattering plane, thereby equalizing the scattered light from each laser. The time separation between laser pulses was set at 4 μs. The laser sheets were generated using a combination of spherical and cylindrical lenses and the resulting sheet thickness was approximately 1.2 mm.

Titanium dioxide (TiO_2) particles were used as seed particles and were introduced upstream of the stagnation chamber of the tunnel by using a two-stage fluidized-bed seeder followed by a cyclone separator (nominal particle diameter quoted by the manufacturer $\approx$ 0.02 μm, however, the agglomerated particle diameter is about 0.2 μm). Time response measurement of the particles through a normal shock indicated that the response time was about 2.6 μs. The Stokes number (is defined as the ratio

between particle response time and a characteristic time scale in the flow) based on the outer time scale of boundary layer ($\delta/U_\infty = 25\,\mu s$) is about 0.1. This suggests that these particles are capable of tracking velocity fluctuations with time scales of δ/U_∞ or higher. Additional details on these particles are given in Ganapathisubramani, Clemens & Dolling (2006, 2007).

The light scattered by the particles was captured by two pairs of CMOS cameras (Photron FASTCAM-Ultima APX) as shown in figure 2. The bottom cameras were synchronized with laser 1 and the top cameras captured the light from laser 2. The images from the bottom cameras were cross-correlated with the corresponding images from the top cameras to obtain PIV velocity fields. This arrangement was utilized in order to maintain a high data rate. Generic HSPIV systems usually expose both laser pulses to the same camera. This will reduce the effective data rate to half the framing rate of the cameras. Since the goal of the current study is to capture the low-frequency unsteadiness of shock-induced separation, a data rate of at least 6 kHz was deemed necessary. Therefore, the aforementioned arrangement was implemented in order to obtain PIV data at 6 kHz (rather than 3 kHz, which would be PIV data rate, if both particle images were acquired by the same camera).

At a framing rate of 6 kHz, these CMOS cameras are only capable of operating at a resolution of 512×512 pixels. The cameras were fitted with Nikon 105 mm lenses ($f/2.8$) and the resulting field of view for a single camera pair was approximately 38×38 mm^2 (magnification factor of 0.074 mm pixel^{-1}). The cameras were slightly de-focused in order to minimize the effects of pixel-locking on the velocity data. The field of view was chosen such that the resulting spatial resolution is sufficient to capture the spanwise organization of the structures in the upstream boundary layer. However, the global characteristics of the interaction cannot be captured with this field of view. Therefore an identical camera pair (as shown in figure 2) was added to the setup to increase the field of view along the streamwise direction. This will effectively improve the spatial dynamic range of the measurements. The wide field of view along the streamwise direction acquired as a result of using two pairs of cameras is approximately 76×38 mm^2.

The cameras were registered using a two-step process. First, the fields-of-view of the top and bottom cameras were matched 'by hand' to within 2–3 pixels. Second, a calibration grid was imaged with both sets of cameras to find the magnification factors and the geometric bias for each interrogation window location. The de-warping coefficients were obtained from a commercial software package (TSI Insight), and these were used to correct the vector fields for the fixed bias between the cameras. The bias error was also determined using an alternate technique and is described later in this section.

A total of 12 000 images were obtained with each camera. These images were processed using TSI Insight 6.0 software which recursively refined the interrogation window from 128×128 pixels down to a size of 32×32 pixels. The final interrogation window corresponds to a spatial resolution of 2.3 mm (0.18δ) in both streamwise and spanwise directions. A 50 % overlap was used to provide a vector field of size 63×32 vectors. The average streamwise pixel displacement in the upstream boundary layer was about 22 pixels. A standard 3×3 neighbourhood median filter with a tolerance of 5 pixels was utilized to remove erroneous vectors. Any missing vectors were interpolated using a 3×3 local mean technique. The number of spurious vectors was less than 5 % in the dataset. The uncertainty in the mean and r.m.s. values of streamwise velocity is approximately 0.5 % and 4.5 %, respectively (this is based on a bias uncertainty of 0.1 pixels in the PIV interrogation).

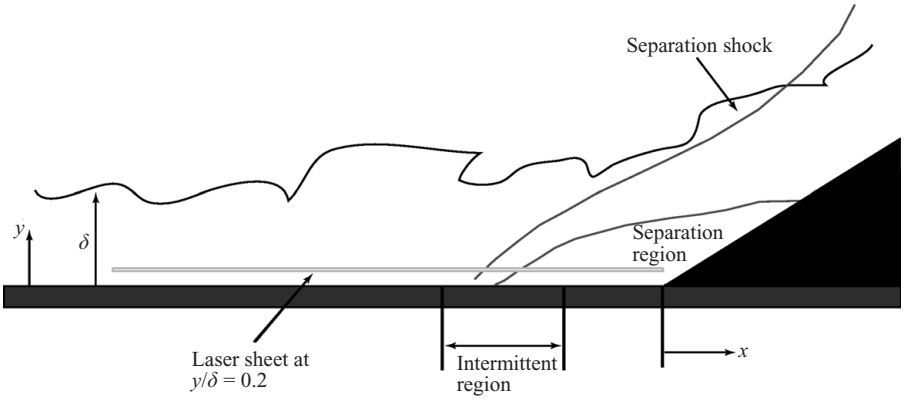

FIGURE 3. Schematic illustration of the compression ramp interaction. Also shown is the streamwise–spanwise laser sheet that is located at $y/\delta = 0.2$.

It must be noted that the aim of this study is to resolve the large-scale low-frequency features of shock-induced turbulent separation, for which the above-mentioned spatial resolution was satisfactory. However, this resolution cannot be used to accurately measure statistics of gradient quantities like vorticity or to identify small-scale vortex cores in the flow field. This resolution is akin to a low-pass filtered velocity field where the emphasis is on the large-scale structures. Spencer & Hollis (2005) suggested that the integral length scale and the r.m.s. velocity fluctuations can be deduced to within 10 % uncertainty for a resolution that is five times smaller than the integral length scale of the flow. In the current study, the resolution is about five times finer than the spanwise integral length scale and over 10 times smaller than the streamwise integral length scale (integral length scales of the upstream boundary layer). Therefore, the relevant spatial scales are well resolved in the present study.

The bias that arises owing to misalignment of the cameras was also measured directly. This was achieved by the following technique: The time separation between lasers 1 and 2 was set to zero (i.e. both laser sheets were fired simultaneously and illuminated the same set of particles). Glycerine-based seed particles were introduced in the test section of the wind tunnel and the light scattered by the particles was captured by both top and bottom cameras simultaneously. The images from the top cameras were correlated with those of the bottom cameras to compute particle displacements. Under ideal circumstances (i.e. if the cameras were perfectly aligned), the displacements should all be identically zero since the time separation is zero. However, since the cameras are not perfectly aligned, the computed displacements give a direct measure of the misalignment for each interrogation window in pixels, which is a bias that was subtracted from the final velocity data.

Measurements were performed in the logarithmic region of the turbulent boundary layer at a nominal wall-normal location of $y/\delta = 0.2$ (2.5 mm from the wall) as shown in figure 3. It must be noted that the laser sheet thickness was approximately 1.2 mm, which results in a measurement volume depth of approximately 0.1δ. This is comparable to the streamwise–spanwise resolution based on the interrogation window size.

3. Results

In all results presented in this section, the coordinates are normalized by the 99 % boundary layer thickness (δ). The velocities are normalized by the free stream velocity (U_∞). The origin in the streamwise direction ($x/\delta = 0$) is located at the corner of the

ramp as shown in figure 3. The origin in the spanwise direction ($z/\delta = 0$) is along the centreline of the test section.

The contour/vector plots depicted in this section are from individual realizations, but the patterns are representative of those found in many vector fields. The statistical results such as correlations and probability density distributions were obtained by investigating all available vector fields (a total of 12 000 vector fields).

3.1. *Upstream boundary layer*

In the first phase of the study the structure of a supersonic turbulent boundary layer was investigated by using HSPIV. These measurements were performed to qualify the upstream boundary layer and to characterize the long coherent structures that were observed in a previous study using low-framing rate PIV (Ganapathisubramani *et al.* 2006). Note that the compression ramp was removed from the test section for these boundary layer measurements. The field of view (with respect to the wind tunnel test section) is identical to the field of view used to study the compression ramp interaction.

Figure 4 is a time sequence of plots that show contours of streamwise velocity obtained using HSPIV at a wall-normal location of $y/\delta = 0.2$. The time between each plot in the sequence is 166 μs during which the flow structures travel across the entire image length. The contours reveal spanwise organization of low- and high-speed regions. The presence of long streamwise structures in the outer part of supersonic boundary layers was previously observed in the current Mach 2 tunnel by Ganapathisubramani *et al.* (2006) as well as in planar laser scattering measurements performed by Samimy, Arnette & Elliot (1994) in another institution's supersonic tunnel.

The streamwise extent of these elongated coherent structures can be investigated by applying Taylor's hypothesis to the HSPIV data. This can be achieved by choosing an image in a sequence as the first block and shifting successive images in the streamwise direction by a distance Δx such that $\Delta x = -U_c \Delta t$ (where $U_c = \overline{U}$ is the convection velocity and $\Delta t = 166\,\mu s$ is the time separation between successive images. It is assumed that the structure convects at a speed equal to the local mean streamwise velocity at this wall-normal location. This is analogous to converting time series data obtained from point measurement techniques into spatial data using Taylor's hypothesis. It must be noted that this procedure is followed to obtain qualitative information on the streamwise extent of these uniform low- and high-speed regions.

Figure 5(*a*) shows a sample image obtained by applying Taylor's hypothesis to acetone fog visualization data (from Ganapathisubramani *et al.* 2007). This visualization technique is distinctly different from PIV as quantitative velocity information cannot be deciphered from the images. However, the images provide qualitative information on the velocity. The image shows the intensity of the light scattered by condensed acetone droplets in the flow. High- and low-signal intensity regions correspond to regions of low and high local static temperature, respectively (the acetone droplets condense and scatter light when the static temperature is low and evaporate when the static temperature is high). This together with the energy equation ($C_p T_o = C_p T + 0.5U^2$, where C_p is the specific heat at constant pressure, T is the local static temperature and U is the local streamwise velocity), indicates that the regions of high- and low-signal intensities correspond to low- and high-speed regions (please see Ganapathisubramani *et al.* 2007 for further details). Figure 5(*a*) clearly shows a high-speed region (region of high-signal intensity at the bottom edge of the image along $z/\delta = 1$) that extends from $x/\delta = -2.5$ to $x/\delta = -40$. However, planar laser scattering essentially provides a concentration map of fog at an instant. Although, the concentration of the fog may be useful as a general proxy for flow

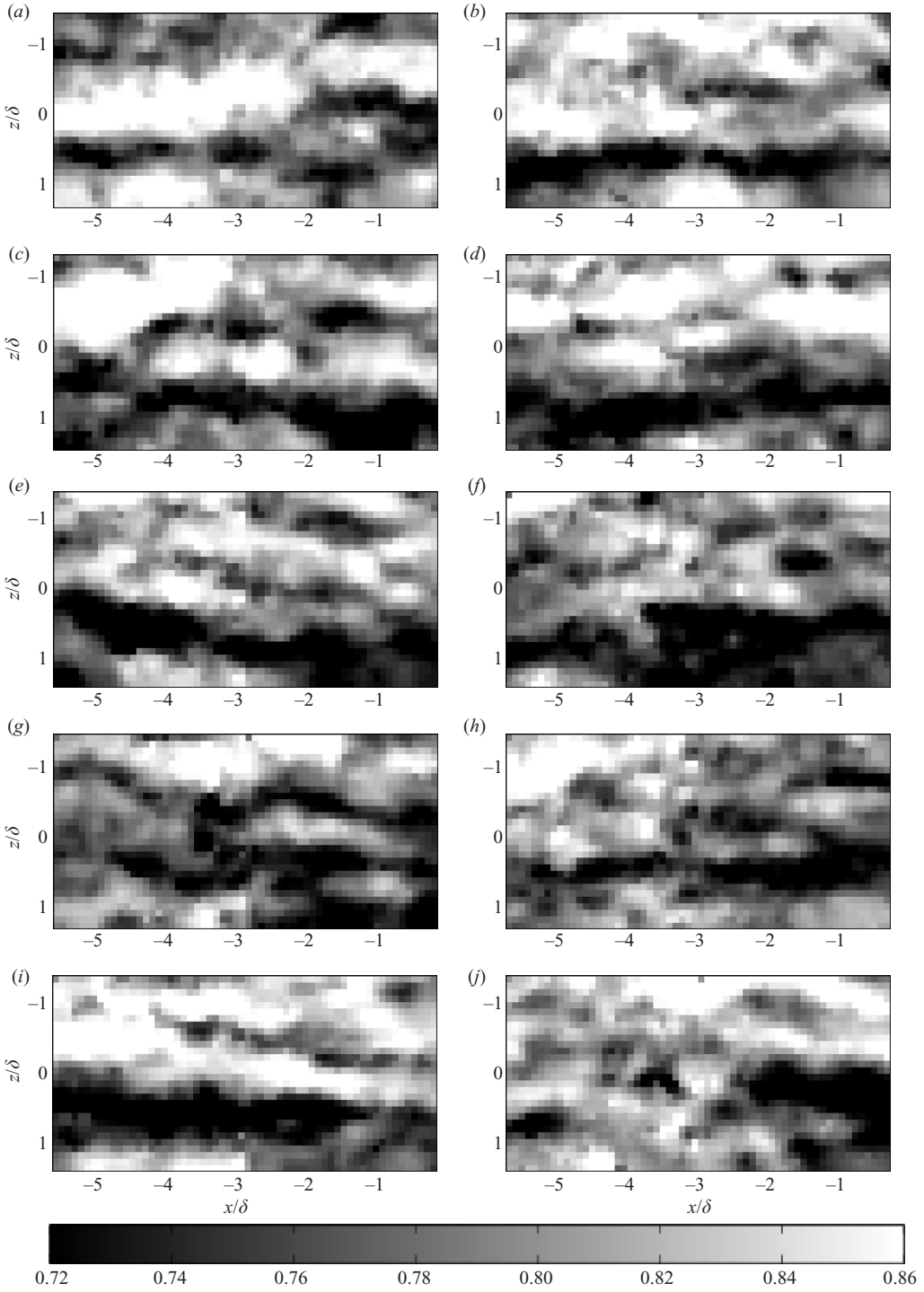

FIGURE 4. Instantaneous streamwise velocity contours at 10 successive time steps. The time separation between successive fields is 166 μs. The streamwise velocity is normalized by the free stream velocity (U_∞). Flow is from left to right.

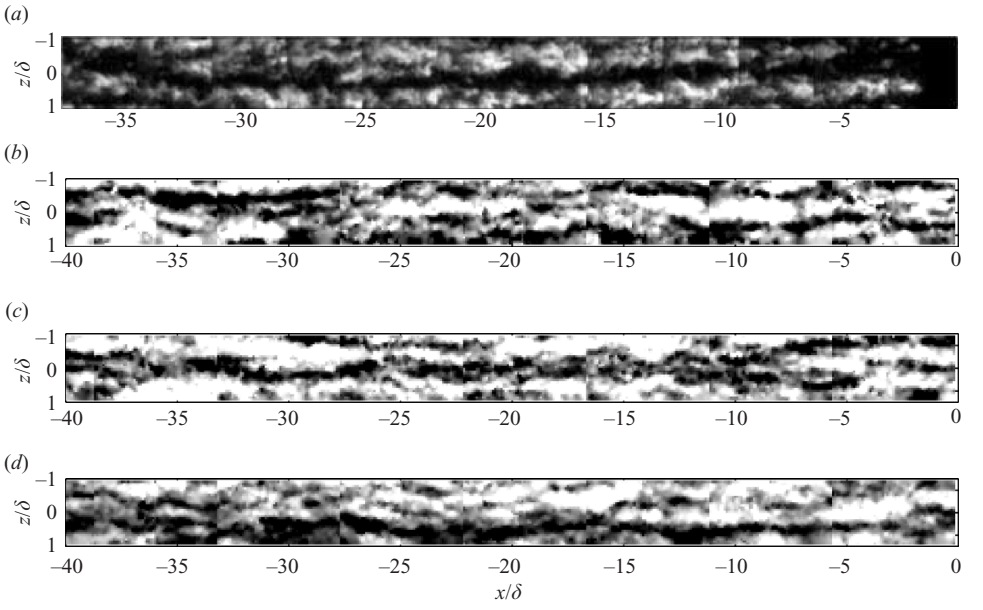

FIGURE 5. Spatial data reconstructed using Taylor's hypothesis. (*a*) Sample planar laser scattering data reproduced from Ganapathisubramani, Clemens & Dolling (2007) at $y/\delta = 0.2$. Successive PLS images are separated by 100 μs. (*b*)–(*d*) Examples of spatial data reconstructed using successive HSPIV vector fields and Taylor's hypothesis at $y/\delta = 0.2$. Successive vector fields are separated in time by 166 μs and a convection velocity of $U_c = \overline{U} = 410\,\mathrm{ms}^{-1}$ is used for reconstruction. The grey scale values vary linearly between $0.7U_\infty$ and $0.9U_\infty$ with decreasing velocity values depicted with increasing black levels. The flow is from left to right.

speed (by using the energy equation), it does not provide accurate instantaneous velocity information. The technique does not account for the finite time required for the condensation of the fog (time required for condensation is unknown) and heat-release effects associated with the condensation process. Therefore, the acetone fog visualization does not provide quantitative velocity information. Hence, application of Taylor's hypothesis to the HSPIV data obtained in the current study would also serve to validate the conclusions by Ganapathisubramani, Clemens & Dolling (2007) based on acetone fog planar laser scattering (PLS) measurements.

Figure 5(*b–d*) shows three examples of spatial data reconstructed from sequences of vector fields using Taylor's hypothesis at $y/\delta = 0.2$. All three examples reveal the presence of elongated strips of low- and high-speed regions adjacent to each other. Figure 5(*d*) shows an elongated low-speed region (at the bottom of the figure) that extends nearly the entire length ($\approx 35\delta$). These elongated structures meander significantly in the spanwise direction. Figure 5(*d*) shows that the 40δ long low-speed region meanders a distance of about $1 - 2\delta$ in the spanwise direction. The regions of uniform speed are similar to those found in incompressible boundary layers by Hutchins & Marusic (2007), where the authors reconstructed the spatial extent using Taylor's hypothesis with time series data obtained using a spanwise rake of hot-wire/sonic anemometers in a variety of boundary layer flows. The observed results are also consistent with recent DNS studies performed by Ringuette, Wu & Martin (2008). The fact that these elongated structures are present in the velocity data also validates the use of PLS to extract qualitative information on velocity fluctuations.

3.2. *Compression ramp interaction*

Details on the mean characteristics of the interaction obtained using low repetition rate PIV data are presented in Ganapathisubramani, Clemens & Dolling (2007). This data indicated that the spanwise organization of the compression ramp interaction is two-dimensional in the mean. However, the interaction is highly three-dimensional instantaneously. The origin of this three-dimensionality will be further explored in this section by using the HSPIV data.

3.2.1. *Local influence*

Figure 6 shows streamwise velocity contours in a streamwise–spanwise plane at $y/\delta = 0.2$ in a compression ramp interaction. The streamwise velocity is normalized by U_∞. The images are separated in time by 166 μs. The structures in the boundary layer convect an entire image length (across the field of view) between successive vector fields. The separation region is located within the black region at the right edge of each image. Although, negative velocities are found in this region in certain instantaneous vector fields, it is not always present. This is primarily due to the fact that the mean separation bubble (and consequently any 'reverse' flow in the mean velocity field) in these type of compression-ramp interactions only extends up to a wall-normal location of $y/\delta \approx 0.1$ (see Settles, Vas & Bogdonoff 1976; Müller, Mümmler & Staudacher (2001). Therefore, in the current study, it is assumed that the separated flow is related to the lowest velocity (black) regions in each image (the low velocities are typically in the range 200–250 ms^{-1}). This assumption is based on results from PIV measurements in streamwise-wall-normal planes where low-velocity contours were found to extend upstream (across all wall-normal locations) when the shock-foot is located farther upstream from the ramp. Similarly, the low-velocity contours are pushed closer to the ramp when the shock-foot is located closer to the ramp (see Hou 2003; Hou *et al.* 2003).

The spanwise organization of the low-velocity region (from hereon referred to as the separation region) in figure 6 is undulated and conforms to the presence of high- and low-speed regions in the upstream boundary layer. The separation region extends far upstream (bottom of figure 6*e*) when the upstream boundary layer has a long low-speed region. Similarly, the separation region is pushed downstream (top of figure 6*e*), when there is a high-speed region in the upstream boundary layer. These findings are consistent with the PLS/PIV results of Ganapathisubramani *et al.* (2007), where the authors found a correlation between the presence of elongated uniform speed regions and a surrogate for the instantaneous location of separation.

The temporal variation in the structure of the separated flow can be observed by inspecting the movie file *movie1.mov*. The movie sequence covers a duration of 1000 outer time scales (i.e. $1000\delta/U_\infty$). The time separation between successive frames is approximately $6.8\delta/U_\infty$. The movie is played at a rate of 5 Hz (i.e. 5 frames s^{-1}). The movie illustrates the fact that the upstream envelope of the separation region is highly unsteady and responds to the passage of elongated regions of uniform speed.

To further quantify the location of the separation region, a threshold-based technique, which identifies a 'surrogate' for the true instantaneous separation, is utilized. Conditional averages obtained by Hou (2003) and Hou *et al.* (2003) showed that low-velocity contours extend farther upstream when the shock-induced separation region is larger and conversely the same velocity contours are pushed downstream when the separation region is smaller. Therefore, a velocity-based threshold technique can be used to locate a surrogate for true separation. However, the value of the

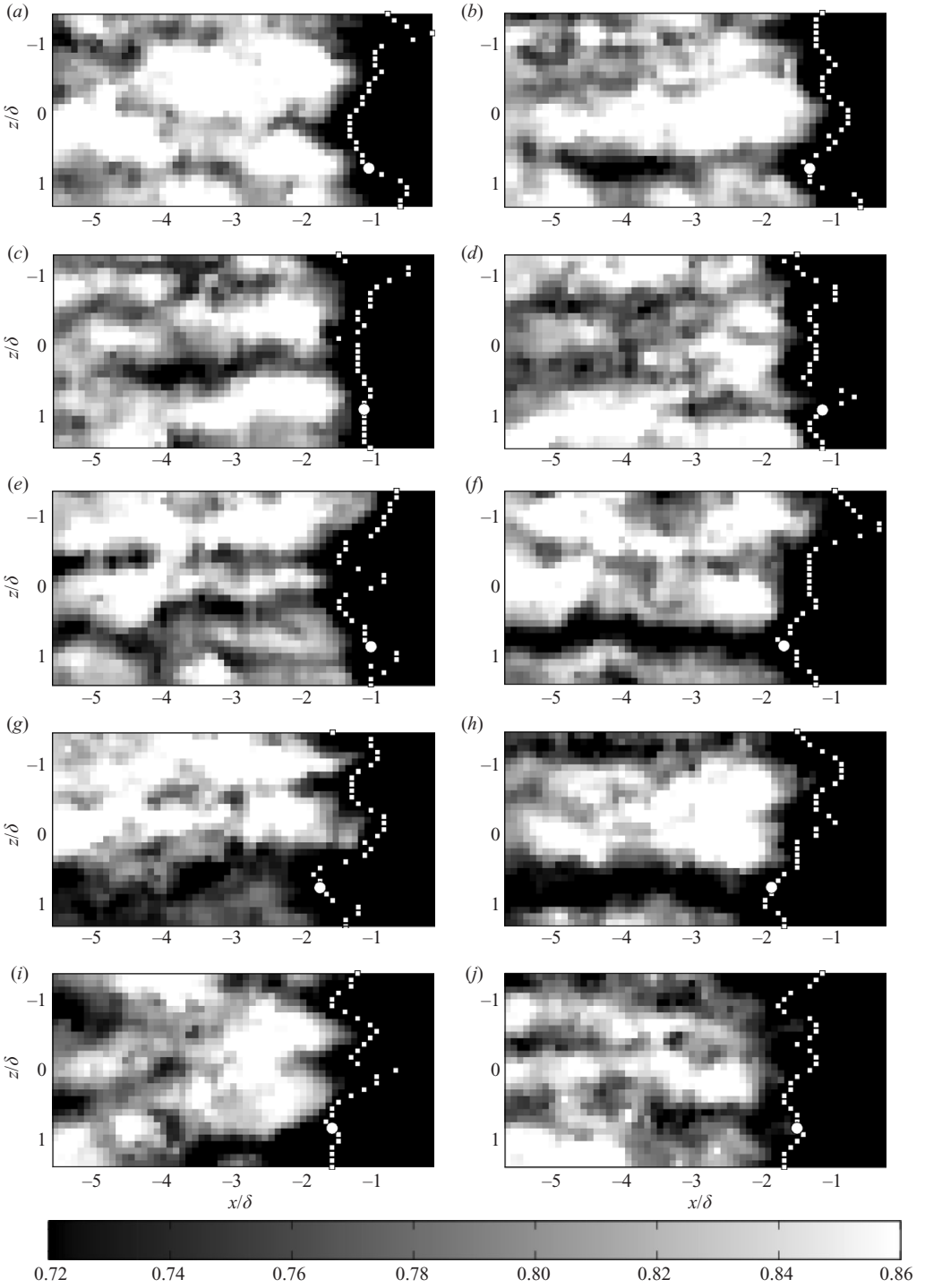

FIGURE 6. A time-sequence of streamwise velocity contours at $y/\delta = 0.2$. Subsequent plots are separated in time by 166 μs. The streamwise velocity is normalized by the free stream velocity (U_∞). Flow is left to right. The 'surrogate' separation point is marked at every spanwise location with a symbol. A particular point on the separation line, marked with a circle symbol, and which is used in subsequent analysis, is also shown.

threshold must be chosen such that the nominal fluctuations in the upstream boundary layer are not identified as 'surrogate' separated flow. Therefore, the threshold was fixed based on the mean and r.m.s. statistics of the upstream boundary layer.

The surrogate for the separation point at a given spanwise position was defined as the streamwise point at which the instantaneous streamwise velocity is less than $U_m - 4\sigma_u$ (i.e. $U < 260\,\mathrm{ms}^{-1}$, where U_m and σ_u are the mean and r.m.s. streamwise velocities of the upstream boundary layer). The mean and r.m.s. of the streamwise velocity in the upstream boundary layer at this wall-normal location were found to be 410 and $35\,\mathrm{ms}^{-1}$, respectively. This streamwise point is identified for every spanwise location. This stringent threshold ensures that the normal variations in velocity in the boundary layer are not falsely identified.

The surrogate separation point (x_{sep}) directly depends on the threshold used to identify it. The identified x_{sep} would be farther downstream if the threshold is decreased to a lower velocity. However, decreasing the threshold would decrease the number of points available for analysis. Therefore, there must be a balance between the threshold used to eliminate false identification and the number of points included in the analysis. Ganapathisubramani *et al.* (2007) explored the effect of threshold on the surrogate separation point in detail and concluded that decreasing the threshold does not alter any observed trends, however, as mentioned previously, it does reduce the number of points included in any analysis. They also indicated that a threshold of $U_m - 4\sigma_u$ performs well at this wall-normal location. Since the primary goal of this study is to investigate the temporal variation of separation, it is important to identify this point in every frame. Therefore, a threshold of $U < U_m - 4\sigma_u$ was used to identify the surrogate separation point (x_{sep}) as a balance between the number of points included in the analysis and false identification.

The relationship between the upstream boundary layer and the surrogate separation point can be investigated by comparing time histories of the surrogate separation point and a representative velocity in the upstream boundary layer. This representative velocity must be chosen with some care. The repetition rate of HSPIV data is only 6 kHz. However, the velocity fluctuations in the upstream boundary layer possess fluctuations at higher frequencies (This is evident based on the fact that the spatial resolution of the data within the PIV field of view is approximately 0.18δ which corresponds to a temporal frequency of approximately 175 kHz based on a convection velocity of $0.8U_\infty$). Therefore, the time history of velocity at any single point in the upstream boundary layer could suffer from aliasing effects. Therefore, a line-averaged velocity is chosen to represent the upstream boundary layer.

This line-averaged streamwise velocity (U_l) is computed along a streamwise line that extends from the identified surrogate separation point to the end of the field of view (on average, the streamwise length over which U_l is computed is approximately 4δ). This line-averaging process acts as a low-pass filter and therefore minimizes the effects of aliasing (see the Appendix for further details). It is assumed that the time history of the surrogate separation point is not affected by aliasing as the dominant frequency range of the separation region is approximately six times lower than the HSPIV acquisition rate. This assumption is based on the results from previous studies that show that wall-pressure fluctuations and mass-flux fluctuations possess significantly higher energy content in the dominant frequency range (see Dussauge *et al.* 2006; it is also seen from the pressure fluctuations in figure 1). Therefore, the effect of aliasing on the time history of surrogate separation point is expected to be minimal.

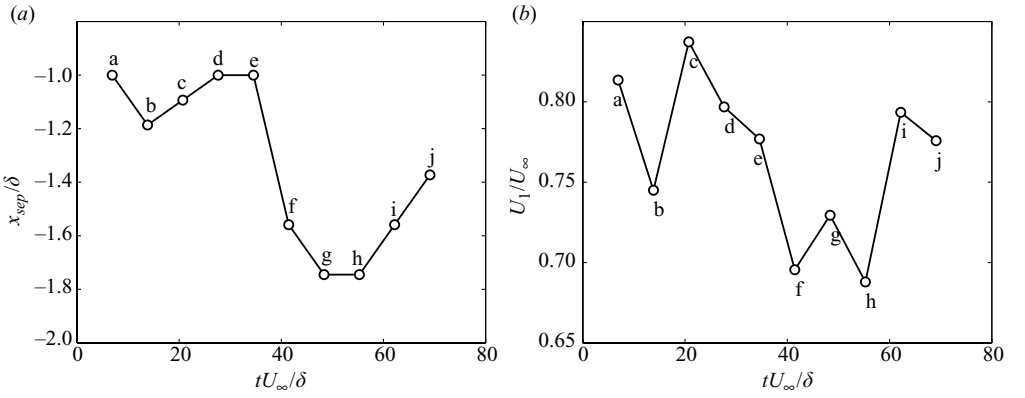

FIGURE 7. (*a*) The instantaneous surrogate separation point at $z/\delta = 0.85$. The point is marked with a '$\circ$' in figure 6(*a–h*). (*b*) The line-averaged streamwise velocity (U_l) in the upstream boundary layer along the line of the surrogate separation point at $z/\delta = 0.85$. The velocity is normalized by the free stream velocity U_∞. The labels on the points correspond to the individual sub-figures in figure 6.

Figures 7(*a*) and 7(*b*) show the time histories of x_{sep} and U_l at a representative spanwise location, $z/\delta = 0.85$ (this point is marked with a '$\circ$' symbol in the sequence shown in figure 6*a–j*). Figure 7(*b*) shows that the time history of U_l exhibits a signature that is similar to the one observed for the surrogate separation point in figure 7(*a*). The upstream boundary layer appears to be locally slowing down between points *c* and *f*. This 'deceleration' region appears to be followed by the upstream motion of the surrogate separation point as seen in figure 7(*a*). Conversely, the line-averaged streamwise velocity increases between points *f* and *g* and that corresponds to the downstream shift of the surrogate separation point in figure 7(*b*). These observations are consistent with the instantaneous contours of streamwise velocity shown in figure 6.

A long time sequence (lasting $1000\delta/U_\infty$) of the motion of the upstream envelope is depicted in the movie file, *movie2.mov*. This movie consists of three different plots. The first plot (upper left) shows the streamwise velocity contours in a streamwise–spanwise plane. The upstream envelope of the separation region is marked using square symbols. The second plot (upper right) reveals the temporal variation of x_{sep} at $z/\delta = 0.85$ (this point is marked with a green square symbol in the first plot). The third plot shows the time history of U_l computed upstream of the point marked with the green square symbol in the first plot. The movie of all three plots together reveal the dynamics of both x_{sep} and U_l and shows that the upstream/downstream motion of the surrogate separation point is correlated to the magnitude of U_l.

Figures 8(*a*) and 8(*b*) show the temporal variation of the instantaneous surrogate separation point and the mean streamwise velocity along a line upstream of the surrogate separation point at $z/\delta = 0.85$, respectively (these time histories are identical to those depicted in the movie, *movie2.mov*). The time axis extends up to 1000 outer time scales. The figures reveal a correlation between the mean streamwise velocity in the upstream boundary layer and the location of the separation.

The relationship between the two time traces can be further explored by computing the temporal correlation between the two signals. The following cross-correlation between the fluctuating components of the two time traces was computed:

$$R_{u_l x_o^f}(\Delta t) = \overline{u_l(t, z) x_o^f(t + \Delta t, z)}, \tag{3.1}$$

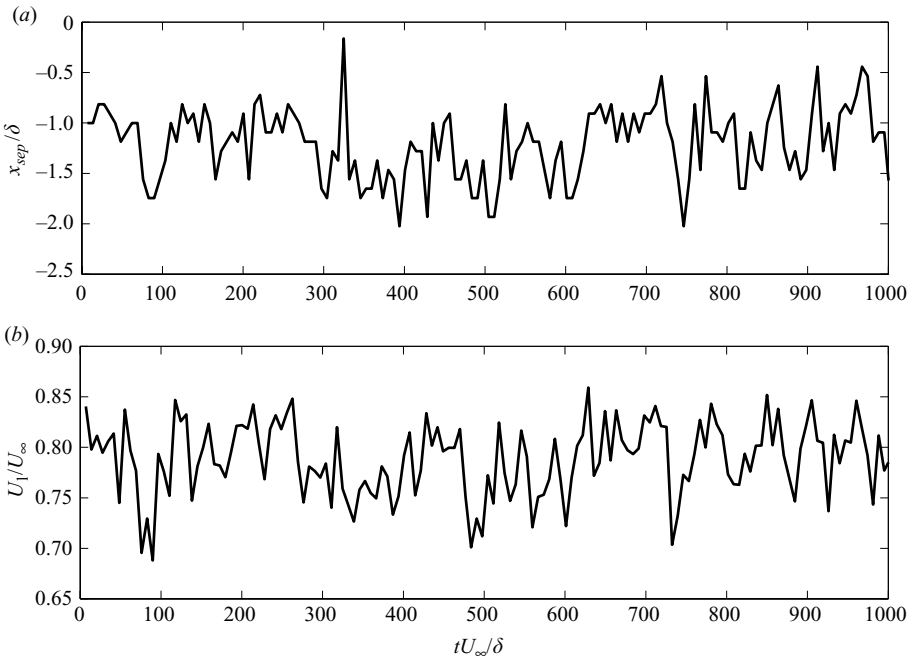

FIGURE 8. Temporal variation of (*a*) the instantaneous surrogate separation point at $z/\delta = 0.85$; (*b*) the line-averaged streamwise velocity (U_l) in the upstream boundary layer along the line of the surrogate separation point at $z/\delta = 0.85$. The velocity is normalized by the free stream velocity U_∞. Note that the time axis plots up to 1000 outer time scales.

where u_l is the fluctuating component of U_l about the mean streamwise velocity of the upstream boundary layer ($u_l = U_l - U_m$). The fluctuating surrogate separation point x_o^f is computed about the overall mean surrogate separation point (which is the spanwise- and temporal-averaged value of x_{sep}). The correlation was normalized by the r.m.s. values of u_l and x_o^f. The correlation was computed for every spanwise position and subsequently averaged, to obtain a smoother temporal correlation curve.

Note that the overall mean value of x_{sep} is negative (due to the choice of the coordinate system in which the origin along the streamwise direction is located at the ramp corner) and therefore a positive value of x_o^f is located downstream (closer to the ramp corner) whereas a negative value of x_o^f is located farther upstream (away from the ramp corner).

Figure 9 shows the above-mentioned correlation between the line-averaged streamwise velocity fluctuation and the corresponding fluctuation of the surrogate separation point. The figure shows that the correlation coefficient at $\Delta t = 0$ is 0.39. The fact that the correlation is positive indicates that the presence of low-/high-speed region in the upstream boundary layer is correlated to the upstream/downstream position for the surrogate separation point. Moreover, the correlation value at $\Delta t = 0$ is consistent with the correlation value computed using instantaneous wide-field PIV data by Ganapathisubramani *et al.* (2007) (the correlation in that study was 0.4). However, figure 9 indicates that the correlation increases to a value of 0.62 at $\Delta t = 6.8\delta/U_\infty$, shedding some valuable insight into the dynamics of unsteadiness. The correlation is found to decrease beyond this point.

The peak at $\Delta t = 6.8\delta/U_\infty$ shows that the surrogate separation point fluctuation lags the line-averaged velocity fluctuation in the upstream boundary layer. However,

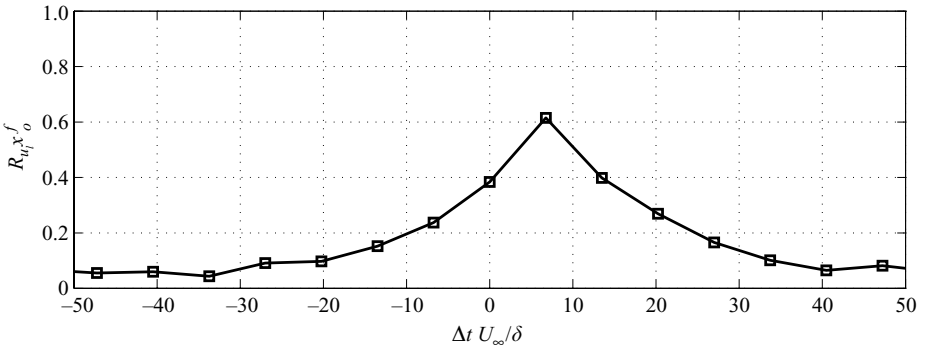

FIGURE 9. Temporal cross-correlation function between the line-averaged streamwise velocity fluctuation ($u_l = U_l - U_m$) and the corresponding fluctuating component of the surrogate separation point ($x_o^f = x_{sep} - \overline{x_{sep}}$). The correlation is computed for every spanwise location and ensemble averaged to obtain a smoother correlation function. The correlation is normalized by the r.m.s. values of u_l and x_o^f.

it should be noted that the lag between them can be identified only up to a resolution of $6.8\delta/U_\infty$ (166 µs, which is the separation between successive PIV images). Higher flow frequencies need to be resolved to capture the detailed temporal response of the upstream envelope to the passage of these elongated regions. Regardless, this lag can be interpreted as follows: A high-speed region (u_l positive) appears in the upstream boundary layer at an instant t. This high-speed region convects downstream and passes through the separation region, which then responds and relocates to a downstream location at $t + \Delta t$. Conversely, the surrogate separation point relocates to an upstream position as a low-speed region (u_l negative) passes through the separation region.

Based on the above interpretation, it can be concluded that the appearance of elongated low-/high-speed regions in upstream boundary layer is correlated to the *motion* of the 'surrogate' upstream envelope. This finding is consistent with the conclusions of Beresh *et al.* (2002), where the motion of the shock foot was found to be correlated with the velocity fluctuations in the upstream boundary layer.

The relationship between the incoming boundary layer and the surrogate separation point can be further explored by smoothing the velocity fields. The vector fields are smoothed by locally averaging each image with its six nearest neighbours (in time). This will have the effect of blurring the high-frequency motions that are captured within the PIV field of view and only leaving the large-scale structures that occur at frequencies of less than 1 kHz. Figure 10 shows a sequence of plots that are smoothed using aforementioned technique. The instantaneous spanwise surrogate separation line is marked in all the plots. The low-frequency response of the surrogate separation line to the presence of elongated regions of uniform speed in the upstream boundary layer is depicted in the sequence. For example, the surrogate separation point at $z/\delta = 0.85$ (marked with a ○ in the plots) gradually moves upstream and this motion corresponds to the appearance of a long low-speed region in the boundary layer.

Additionally, the above observations can also be made in movies of the sequences. The attached movie file, *movie3.mov*, is a running-averaged movie sequence that corresponds to the instantaneous sequence depicted in *movie1.mov*. The movie shows the response of the upstream envelope of the separation region to the presence of low- and high-speed regions in the upstream boundary layer. This provides further evidence that the upstream boundary layer structures drive the large-scale motion of

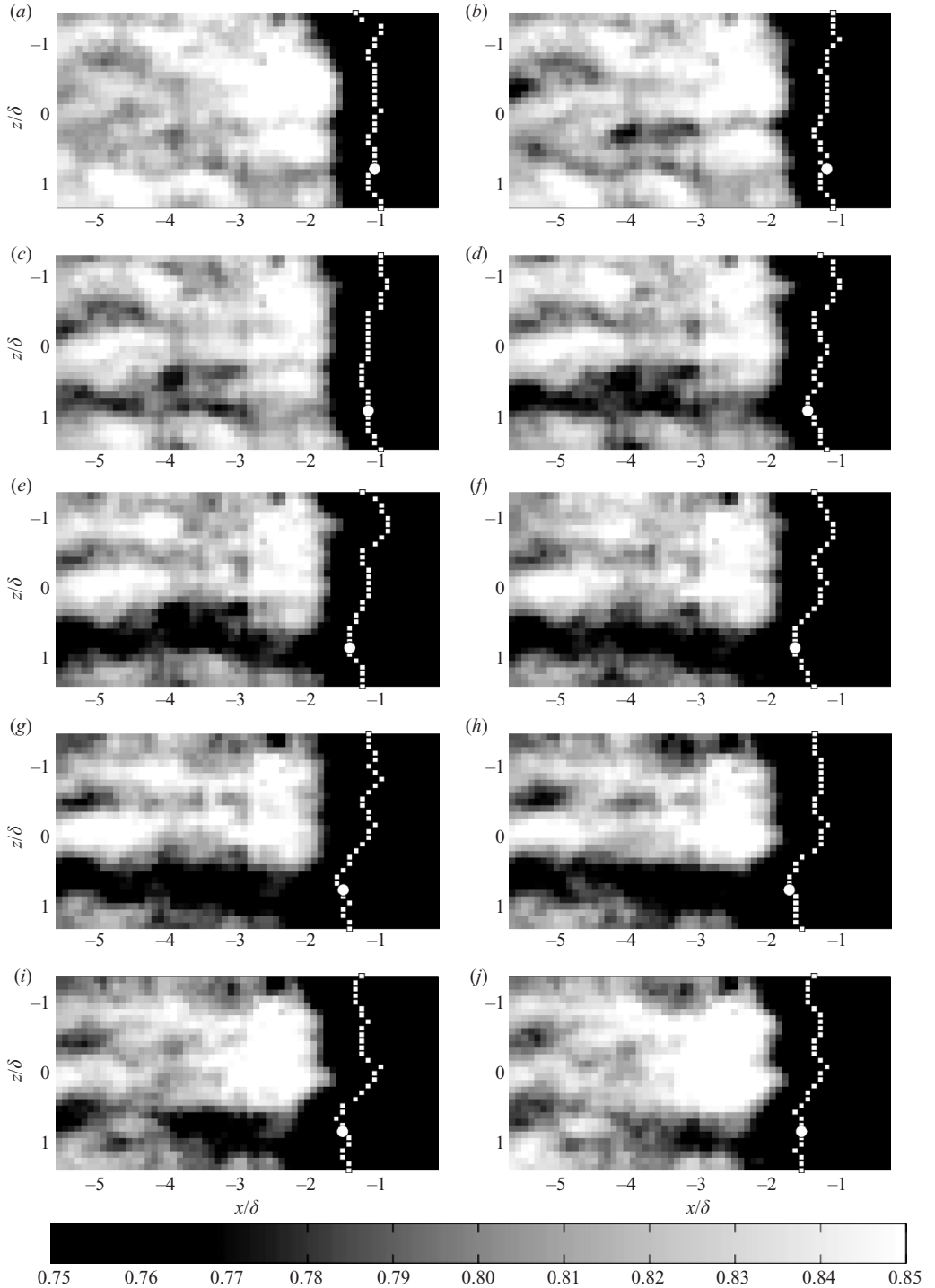

FIGURE 10. A sequence of running-averaged streamwise velocity contours at $y/\delta = 0.2$. Subsequent plots are separated by 166 μs. The vector fields are filtered by computing a six-frame running average. The streamwise velocity is normalized by the free stream velocity (U_∞). Flow is left to right.

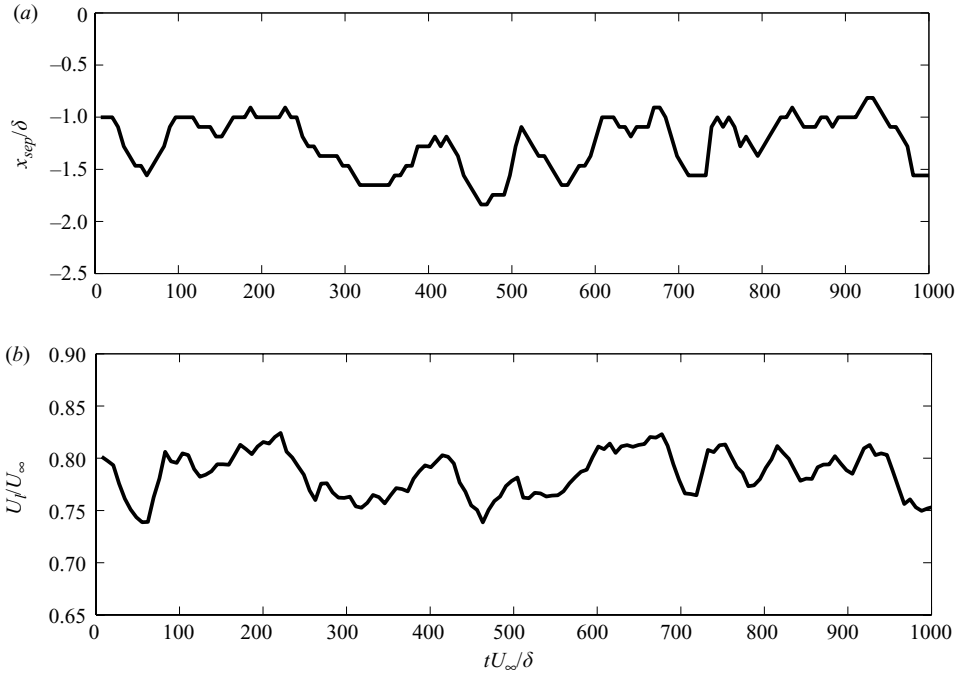

FIGURE 11. Time histories from running-averaged data. (*a*) Surrogate separation point and (*b*) line-averaged streamwise velocity along a streamwise line upstream of the surrogate separation point (U_l). The velocity is normalized by the free stream velocity (U_∞).

the separation region. This conclusion is consistent with previous studies performed with cylinder interactions in a Mach 2 flow by Bueno *et al.* (2005).

It must be noted that a velocity vector at any given point in the upstream boundary layer could still suffer from aliasing effects. The running-average filter does not minimize the effects of aliasing. Therefore, in order to further explore the above-mentioned low-frequency motion of the surrogate separation point and its relationship with the upstream boundary layer, we investigate a long-time sequence of both the surrogate separation point and U_l (line-averaged streamwise velocity). This line-averaged streamwise velocity obtained from the running-average filtered data does not suffer from aliasing effects (see the Appendix). The movie file *movie4.mov* shows running-averaged streamwise velocity contours in a streamwise–spanwise plane, the temporal variation of x_{sep} and U_l (both obtained from the running-averaged data) at a spanwise location of $z/\delta = 0.85$ (marked with a green square symbol). The sequence lasts approximately 1000 outer time scales. The time interval between successive frames is 166 μs ($6.8\delta/U_\infty$). The running-average filter enhances the observed correlation between the motion of x_{sep} and U_l.

Figures 11(*a*) and 11(*b*) show the temporal variation of x_{sep} and U_l obtained from the running-averaged data. The figures indicate that the two signals exhibit remarkable similarity. The upstream boundary layer is seen to be fast when surrogate separation point occurs at a downstream location, whereas it is slow when surrogate separation point occurs at an upstream location.

To further quantify this relationship, the correlation coefficient between the two signals was computed. This correlation is similar to the correlation function depicted in figure 9, which was computed using the unfiltered data. Figure 12 shows the

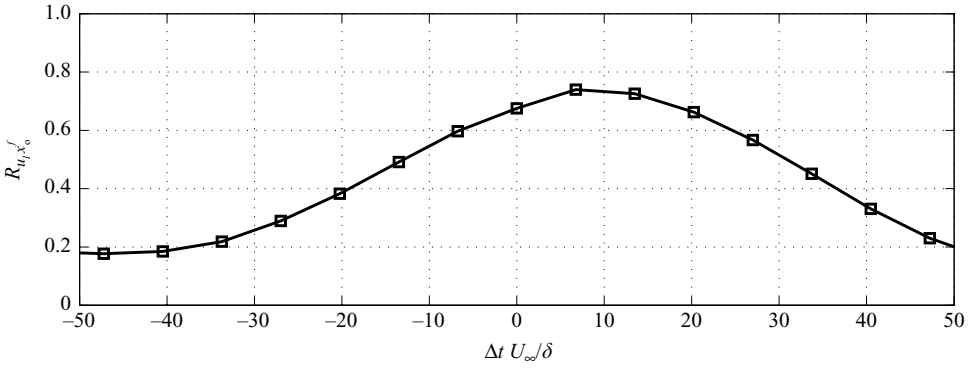

FIGURE 12. Temporal cross-correlation function computed using the running-averaged data. The correlation between line-averaged streamwise velocity fluctuation ($u_l = U_l - U_m$) and the corresponding fluctuating component of the surrogate separation point ($x_o^f = x_{sep} - \overline{x_{sep}}$). The correlation is computed for every spanwise location and ensemble averaged to obtain a smoother correlation function. The correlation is normalized by the r.m.s. values of u_l and x_o^f.

correlation function between the line-averaged streamwise velocity fluctuation and the corresponding surrogate separation point fluctuation computed using the running-average filtered data. The correlation value at $\Delta t = 0$ is 0.7, which is higher than the corresponding correlation value computed using the raw data. Moreover, the peak in the correlation function is located at $\Delta t = 6.8\delta/U_\infty$ and its value is 0.78. This correlation value is higher than the value obtained using the unfiltered data.

3.2.2. *Global influence*

The elongated low- and high-speed regions appear to have an effect on the unsteadiness of shock-induced separation. This effect is local and changes with the spanwise location. However, inspection of time histories of spanwise-averaged surrogate separation point indicates an overall variation. For example, Figure 13(*a*) shows a time history of the spanwise-averaged surrogate separation point (x_{msep}), which is computed by averaging the surrogate separation point along the spanwise direction in every instantaneous vector field. This averaging should remove the local variations of the surrogate separation point and will decrease the range of unsteadiness (in length). The mechanism responsible for this global variation (i.e. variation in the spanwise-averaged surrogate separation point) can be explored by inspecting individual vector fields that possess the observed global change.

Figures 13(*b*) and 13(*c*) show two instantaneous examples that illustrate the global variation of the surrogate separation point. Figure 13(*b*) shows the streamwise velocity contours at an instant that corresponds to a point marked with a '○' in figure 13(*a*). At this instant, the spanwise-averaged surrogate separation point is present at a downstream position (closer to the ramp corner). The instantaneous surrogate separation points are marked with square symbols. The spanwise-averaged surrogate separation point at this instant is at $x_{msep} = -0.8\delta$. Figure 13(*b*) shows that the instantaneous surrogate separation point is indeed undulated corresponding to the low- and high-speed regions. However, the spanwise-averaged surrogate separation point is at a farther downstream position. The streamwise velocity contours in the incoming boundary layer (say, upstream of $x/\delta = -4$, black line in the figure) appear to be dominated by high-speed regions. This suggests that the overall velocity of

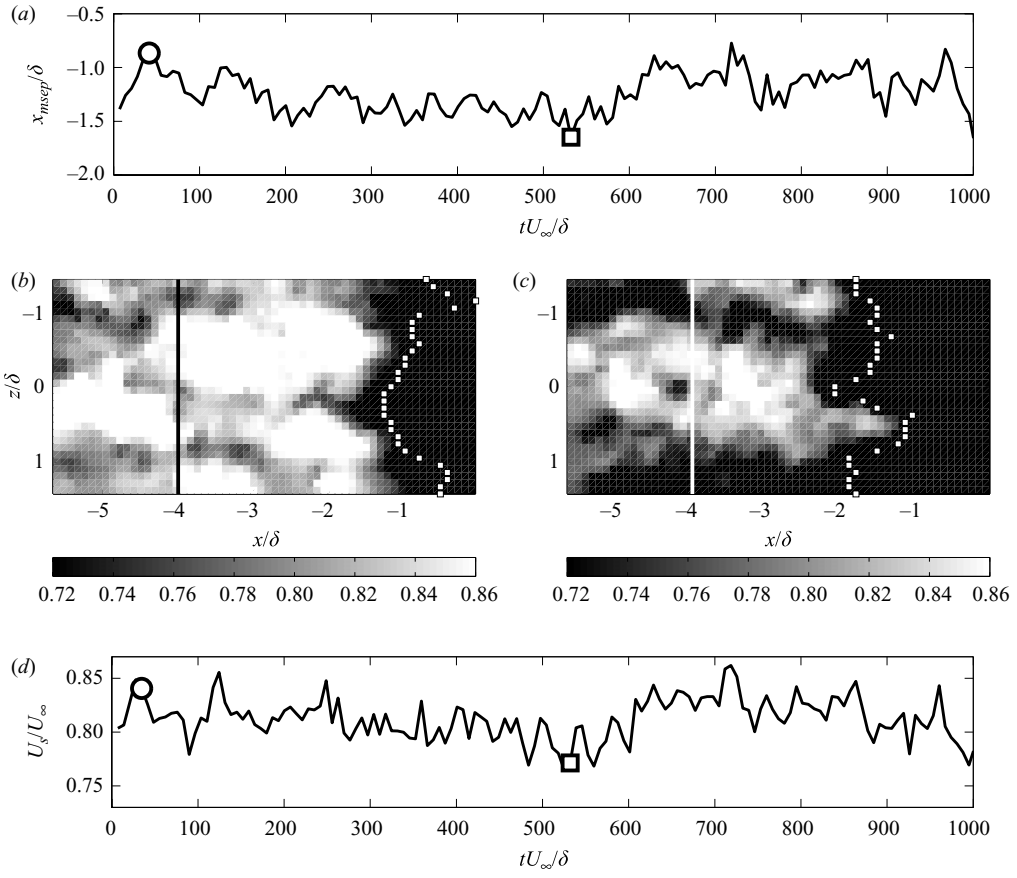

FIGURE 13. Global effect of the upstream boundary layer on the surrogate separation point. (*a*) Time history of spanwise-averaged surrogate separation point (x_{msep}). (*b*) Streamwise velocity contour plot that corresponds to the instant marked with a circle symbol in figure 13(*a*). The representative velocity of the incoming boundary layer is faster than the overall mean (i.e. $U_s > U_m$). (*c*) Streamwise velocity contour plot that corresponds to the instant marked with a square symbol in figure 13(*a*). The representative velocity of the incoming boundary layer is slower than the overall mean (i.e. $U_s < U_m$). (*d*) Time history of the representative velocity (U_s). All velocities are normalized by the free stream velocity (U_∞).

the incoming boundary layer is higher. Perhaps, consequently, the global surrogate separation point is at a farther downstream position.

Figure 13(*c*) shows an example, where the spanwise-averaged surrogate separation point is at an upstream position. This example corresponds to the instant marked with a square symbol in figure 13(*a*). The spanwise-averaged surrogate separation point at this instant is located at $x_{msep} = -1.6\delta$. Examination of streamwise velocity contours in the incoming boundary layer (upstream of $x/\delta = -4$, white line in the figure) indicates that the upstream boundary layer is predominantly slow. This global influence can also be seen in the movie generated using the running-averaged data (*movie3.mov*) where the overall increase/decrease in the average streamwise velocity of the upstream boundary layer is related to the downstream/upstream position of the spanwise-averaged surrogate separation point.

The influence of the incoming boundary layer on the global variation of the surrogate separation point can be further explored by computing a representative velocity for the incoming boundary layer. This representative velocity (U_s) is the mean velocity (mean computed in both streamwise and spanwise directions) of the boundary layer, upstream of $x/\delta = -4$. The representative velocity (U_s) for figure 13(b) is $0.84U_\infty$, which is faster than the overall mean (U_m, which is approximately $0.8U_\infty$). This suggests that the incoming boundary layer possesses a higher velocity at this instant. The representative velocity for figure 13(c) is $0.77U_\infty$, which is slower than the overall mean.

Figure 13(d) shows the time history of U_s that corresponds to the time history of x_{msep} in figure 13(a). The figure shows that the temporal variation of U_s is closely related to the variation of x_{msep}. The two signals reveal a remarkable degree of similarity. The representative velocity indicates a variation of approximately $50\,\mathrm{ms}^{-1}$ ($\pm 0.05U_\infty$) and the spanwise-averaged surrogate separation point varies between -1.8δ and -0.8δ. A closer examination of these two figures shows that a downstream position for x_{msep} is preceded by a gradual decrease in U_s, suggesting that the motion of x_{msep} is related to the variation in the streamwise velocity of the incoming boundary layer.

The above discussion suggests that there is a global influence of the upstream boundary layer on the surrogate separation point, in addition to the local effect discussed in the previous section. However, it is worth noting that the representative velocity (U_s) includes the contributions from the elongated regions of uniform low/high speed. Conversely, the line-averaged streamwise velocity (U_l) discussed in the previous section includes the effect of the overall changes in the boundary layer. Alternately, it could be speculated that the overall increase/decrease in the representative velocity is also an effect of these elongated regions of uniform speed that are much larger than those described in the previous sections.

The global influence could be also dependent on the field of view of the measurement domain. It is conceivable that for a larger field of view (specifically a larger spanwise domain), the perceived global influence might in fact be a local influence at a larger scale. Tomkins & Adrian (2003) suggested a spanwise-scale growth of coherent structures where adjacent structures merge to form a larger structure. Therefore, it is conceivable that neighbouring low- and high-speed regions merge and produce a much larger global structure of low- and high-speed regions. This global structure may be responsible for the overall variations in the velocity of the upstream boundary layer (in addition to the local variations arising due to the strips of uniform speed).

Another influence that could affect the overall characteristics of the boundary layer is free stream turbulence that could potentially induce a similar effect, where the overall boundary layer is faster/slower depending on the free stream turbulence intensity. However, recent results from Weiss & Chokani (2007) suggest that free stream conditions may not be responsible for these variations. Regardless of the exact source, it is increasingly clear that the upstream boundary layer does indeed play an important role on the dynamics of shock-induced turbulent separation.

Dussauge (2001) listed three possible influences that could contribute to the unsteadiness observed in shock-boundary layer interactions: (a) The turbulence structure of the incoming boundary layer, (b) the independent characteristic time and length scales of the separated flow and (c) the unsteady upstream and downstream conditions that could make the shock fluctuate according to its own frequency response. The current study presents strong evidence that highlights the influence of the upstream boundary layer on the dynamics of shock-induced separation. However,

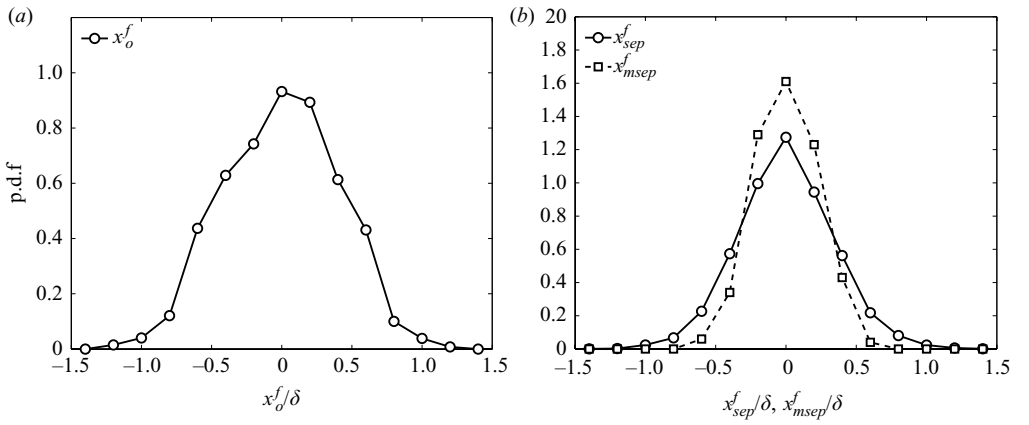

FIGURE 14. Probability density distributions of (*a*) x_o^f, fluctuations of instantaneous surrogate separation point about a time- and spanwise-averaged mean surrogate separation point, (*b*) $x^f{}_{sep}$, fluctuation of instantaneous surrogate separation point about a spanwise-averaged surrogate separation point and $x^f{}_{msep}$, fluctuations of instantaneous spanwise-averaged surrogate separation point about a time- and spanwise-averaged mean surrogate separation point.

the impact of the separation region and response of the shock should not be ignored, and it is possible that the temporal variation of the spanwise-averaged surrogate separation point (x_{msep}) possesses contributions from those other influences.

4. Discussion

Detailed analyses and investigation of time histories of the surrogate separation point (which is a surrogate for the separation point and is computed using a velocity threshold) suggest that the influence of the upstream boundary layer on the unsteadiness of the separated flow may be two-fold. First, a local influence where the local undulation in the spanwise separation line depends on the presence of elongated high-/low-speed regions in the upstream boundary layer. Second, a global influence where the spanwise-averaged surrogate separation point possesses a temporal variation that depends on the global variation of the average streamwise velocity in the incoming boundary layer.

Figure 14(*a*) shows the probability distribution of the fluctuations of the instantaneous surrogate separation point (x_o^f). The distribution shows that the instantaneous surrogate separation point fluctuations range between -1.2δ and $+1.2\delta$. This distribution is consistent with the distributions obtained in Ganapathisubramani *et al.* (2007) at a comparable wall-normal location using wide-field PIV measurements. The variation in the surrogate separation point includes both the local and the global influences of the upstream boundary layer. A robust method to distinguish between the two contributions is not clear. However, one possible technique that can be used to separate the contributions is to compute the fluctuations of x_{sep} and x_{msep}. The local influence can be deduced by computing the fluctuation of the surrogate separation point at every spanwise location about the spanwise-averaged surrogate separation point at that instant.

$$x^f{}_{sep}(z, t) = x_{sep}(z, t) - x_{msep}(t), \tag{4.1}$$

where $x^f{}_{sep}(z, t)$ is the fluctuation at any given spanwise location z, at a time instant t, about the spanwise-averaged surrogate separation point at the same instant $x_{msep}(t)$. This quantity is expected to remove the global variation of the surrogate separation point since the fluctuation is computed about the spanwise mean at every instant and therefore would reveal the impact of the local influence of the upstream boundary layer on the surrogate separation point.

Similarly, the contribution from the global influence can be computed by evaluating the fluctuation of x_{msep} about the overall mean surrogate separation point (which is the time-averaged value of x_{msep}).

$$x^f{}_{msep}(t) = x_{msep}(t) - \overline{x_{msep}}, \tag{4.2}$$

where $x^f{}_{msep}(t)$ is the fluctuation of the spanwise-averaged surrogate separation point at any instant about the overall mean surrogate separation point. This quantity would reveal the temporal variation of the spanwise-averaged surrogate separation point. The fluctuation of the spanwise-averaged surrogate separation point contains the local fluctuations and it may not be feasible to separate the two. However, the local fluctuation $x^f{}_{sep}$ is free from the overall changes in the surrogate separation point since the fluctuation is computed about the instantaneous spanwise-averaged surrogate separation point.

Figure 14(b) shows the probability distributions of both $x^f{}_{sep}$ and $x^f{}_{msep}$. The distribution of $x^f{}_{sep}$, which shows the impact of the local influence on the surrogate separation point, possesses a range of $\pm 1.2\delta$, which is only slightly smaller than the range for x_o^f. It must be noted that the range of the distribution in $x^f{}_{sep}$ is comparable to the range observed in x_o^f in figure 14(a). This suggests that the local influence of the upstream boundary layer makes a key contribution to the three-dimensionality and the unsteadiness of shock-induced separation. The r.m.s. value for this distribution is approximately 0.35δ.

The distribution of $x^f{}_{msep}$ shown in figure 14(b) varies between -0.8δ and $+0.8\delta$. It is seen that the distribution for $x^f{}_{msep}$ possesses much shorter tails compared to the distribution of $x^f{}_{sep}$, suggesting that the temporal variation of the spanwise-averaged surrogate separation point has a shorter range compared to the local and overall variation of the surrogate separation point. The r.m.s. value of $x^f{}_{msep}$ is 0.2δ and is about 1.5 times lower than the r.m.s. value of $x^f{}_{sep}$. This indicates that at this wall-normal location ($y/\delta = 0.2$), the local variation in the spanwise profile of the surrogate separation point is larger than the variation of spanwise-averaged surrogate separation point. Based on this, it may be concluded that the local influence of the upstream boundary layer is stronger than the global influence.

Recently, Humble *et al.* (2009) performed tomographic PIV in a reflected shock/boundary-layer interaction and proposed a model for the low-frequency unsteadiness that is consistent with the results presented in the current study. The authors found that instantaneous reflected shock-wave pattern conformed to the low- and high-speed regions as they enter the interaction and speculated that the low-frequency shock-wave motion can be reconciled by a mechanism involving these large-scale regions.

The findings in the current study do not seem to be consistent with the DNS-based results of Wu & Martin (2008). In their study, the authors track the motion of the shock in the free stream and compare that to the characteristics of the upstream boundary layer and find only a weak correlation between the velocity fluctuations in the upstream boundary layer and the shock motion. They found that the local

corrugations of the shock front in the outer part of the boundary layer ($y/\delta = 0.9$) were minimal when compared to the large variations in the spanwise-averaged shock position (the local corrugations had a larger magnitude at $y/\delta = 0.9$ compared to $y/\delta = 2$). This finding led them to conclude that the elongated low- and high-speed regions in the upstream boundary layer may not be responsible for the low-frequency unsteadiness. The inconsistency between the present study and the results of Wu & Martin (2008) could be due to the differences in the analysis techniques between the two studies. Alternately, the differences could be due to Reynolds number effects where the DNS results are obtained at low Reynolds numbers ($Re_\theta \approx 2000$) while the current experiments are performed at much higher Reynolds numbers ($Re_\theta \approx 40\,000$).

5. Conclusions

High-speed (6 kHz) PIV measurements were performed in streamwise–spanwise planes of a shock-wave turbulent boundary layer interaction generated by a 20° ramp in a Mach 2 flow. Velocity fields of the upstream boundary layer in the log region ($y/\delta = 0.2$) reveal elongated regions of low- and high-speed fluids that extend to streamwise lengths greater than 30δ (length is computed based on Taylor's hypothesis). The presence of elongated low- and high-speed regions in the velocity fields validates the use of PLS data as a qualitative marker for velocity (Ganapathisubramani *et al.* 2007).

HSPIV measurements of the interaction capture a considerable part of the upstream boundary layer and the separation region upstream of the compression ramp. These measurements provide access to time sequences of instantaneous velocity fields, show the presence of long high- and low-speed regions in the upstream boundary layer and the instantaneous spanwise separation line of the shock-induced separation region is seen to be undulated, conforming to the presence of high- and low-speed regions in the upstream boundary layer. Temporal correlation between the line-averaged velocity fluctuation and the surrogate separation point fluctuation indicates a lag between the two quantities, which can be interpreted as a cause and effect relationship. That is, the passage of low-speed (high-speed) regions through the separated flow results in the upstream (downstream) motion of the separation line.

Locally averaged sequences of the velocity fields also reveal strong correlation between the upstream boundary layer and the location of separation and lend further support to previous observations noted by Ganapathisubramani *et al.* (2007) that elongated low- and high-speed regions in the boundary layer is a turbulent mechanism that can account for the low-frequency unsteadiness of the shock-induced separation region. This local motion of the separated flow, which is attributed to the presence of superstructures, is classified as the *local influence* of the upstream boundary layer.

Additionally, the spanwise-averaged surrogate separation point is found to possess a temporal variation. This overall variation is classified as the *global influence* of the upstream boundary layer. It must be noted that this overall variation includes the local effects of elongated low- and high-speed regions in the upstream boundary layer and could include contributions from the inherent unsteadiness of the separation region.

Investigation of fluctuations of the surrogate separation point suggests that the local influence dominates the spanwise variation of the separation line surrogate, contributing nearly 50 % more than the global influence. Regardless, the low-frequency unsteadiness of the separation region can be attributed to a combination of both the *local* and *global* influences of the upstream boundary layer.

We thank Justin Wagner, Zachary Murphree, Bulent Yuceil and Priti Mishra for their help in the data acquisition phase of the study. We also thank an anonymous referee for pointing out the aliasing issue. We are extremely grateful to Mirko Gamba for the useful discussions that enabled us to address the aliasing issue. Finally, the support of the Air Force Office of Scientific Research under grant FA9550-04-1-0387 is gratefully acknowledged.

Appendix. Aliasing effects

The HSPIV data in this study is acquired at a non-dimensional frequency of $6.8\delta/U_\infty$ (i.e. 6 kHz). This frequency is sufficient to capture the low-frequency unsteadiness of the separation region, however, it is important to understand the extent to which the velocity fluctuations in the upstream boundary layer may be aliased. The velocity measurements within the PIV field of view are reasonably well resolved (the captured frequency is approximately 175 kHz based on the interrogation window size of 2.3 mm and the mean streamwise velocity 410 ms^{-1}). However, the fact that there is a discrepancy between the data acquisition rate (6 kHz) and the bandwidth of the PIV interrogation window (175 kHz) raises a concern that the temporal fluctuations of the upstream boundary layer could suffer from aliasing effects.

In the current study, all quantitative analyses that involve the upstream boundary layer velocity fluctuations are based on a line-averaged streamwise velocity component (U_l). This line-averaged velocity does not suffer from aliasing effects as the line-averaging process acts as an efficient low-pass filter. The purpose of this appendix is to show that line averaging is an effective low-pass filter that minimizes aliasing effects that may be present in under-sampled HSPIV data.

Well-resolved hot-wire data obtained in the log region of an incompressible turbulent boundary layer is utilized in this appendix to show that the line-averaging process is an effective low-pass filter. This hot-wire data set was obtained in the high-Reynolds-number boundary layer wind tunnel facility at the University of Melbourne. The details of the boundary layer explored in this experiment are as follows: free stream velocity, $U_\infty = 20\,\mathrm{ms}^{-1}$, 99 % boundary layer thickness, $\delta = 26$ cm and the Reynolds number based on momentum thickness, $Re_\theta = U_\infty\theta/\nu \approx 38\,000$ (this is comparable to the Reynolds number of the supersonic boundary layer explored in the current study). The data used in this appendix was obtained at a wall-normal location of $y/\delta = 0.2$. This data is manipulated to simulate the characteristics of the HSPIV measurements.

A representative integral time scale of the boundary layer is chosen as the reference scale to match the characteristics of the hot-wire data to that of the PIV measurements presented in this study. The integral length scale along the streamwise direction based on the streamwise velocity (Λ) of the supersonic boundary layer explored in the current study is approximately 1.5δ (based on full-width at half the maximum value of the auto correlation function; see Ganapathisubramani *et al.* 2006). This integral length scale can be converted to an equivalent representative integral time scale (T_p) by using a reference velocity, i.e. $T_p = \Lambda/U_\infty$.

The characteristics of the PIV measurements presented in this manuscript based on the above-mentioned representative integral time scale of the upstream boundary layer are as follows: The interrogation window size $w = 0.18\delta = 0.12\Lambda$ is equivalent to $0.12T_p$, vector spacing (with 50 % overlap) is equivalent to $0.06T_p$. The PIV field of view $\mathrm{FOV} = 6\delta = 4\Lambda$ is equivalent to $4T_p$ and the PIV sampling rate $f_s = 6.8\delta/U_\infty = 4.5\Lambda/U_\infty$ corresponds to $4.5T_p$. Finally, the line-averaged streamwise

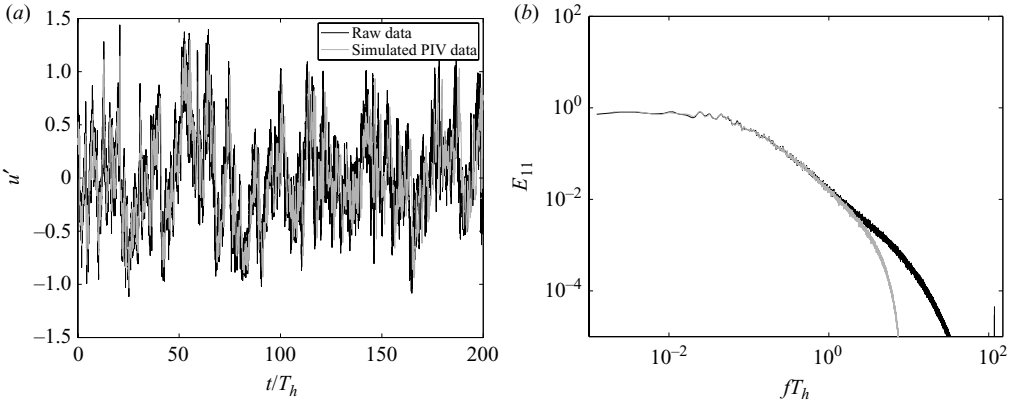

FIGURE 15. A comparison between fully resolved hot-wire data and simulated PIV data (where simulated PIV data is obtained by filtering and resampling the hot-wire data to match the resolution and sampling of a PIV vector field). (*a*) Time trace and (*b*) energy spectra.

velocity is computed by averaging over a distance of approximately $4\delta = 2.67\Lambda$ (equivalent to $2.67T_p$).

The hot-wire data was acquired at a sampling frequency of 20 kHz. This sampling rate corresponds to $0.003T_h$ (where T_h is the representative integral time scale of the hot-wire data computed based on full width at half the maximum value of the auto-correlation). The vector obtained within a PIV interrogation window is an average velocity of the particle pairs within the window. Therefore, in order to match the resolution of the well-resolved hot-wire data to that of the PIV data set, the hot-wire data must be filtered at a scale equivalent to the PIV interrogation window. This can be achieved by applying a moving average filter (of length of $0.12T_h$) over the hot-wire velocity time trace. This ensures that the effective resolution of the velocity at each point is equivalent to that of the PIV interrogation window. The resulting signal is resampled at $0.06T_h$ intervals to simulate the 50 % overlap condition that is enforced in PIV interrogation. This will provide a hot-wire time trace where successive velocity samples possess a resolution and spacing that is equivalent to an instantaneous PIV velocity field. Figure 15(*a*) shows a comparison between the original hot-wire signal and the signal that is filtered and resampled to simulate the PIV data. Figure 15(*a*) reveals minimal differences in the time trace of the two signals and indicates that the modified hot-wire signal accurately captures the low-frequency fluctuations present in the data. Figure 15(*b*) shows the energy spectra of the two signals and clearly indicates that the effects of modifying the hot-wire data are only felt in the high-frequency region (i.e. $fT_h > 4$, this is equivalent to a time scale of $0.25T_h$). The energy content and roll-off of the spectrum in the inertial range and in the lower frequencies are left unchanged (i.e. no aliasing is present).

The modified hot-wire signal together with Taylor's hypothesis is used to arrange the data into successive $4T_h$ long blocks separated in time by $4.5T_h$ as shown in figure 16. This is akin to the adjacent arrangement of successive 6δ long HSPIV vector fields that are separated in time by $6.8\delta/U_\infty$ as shown in figure 5. This rearranged data is used to explore the effects of aliasing on under-sampling the velocity information at a frequency that corresponds to time scale of $4.5T_h$.

The quantitative analyses performed in § 3.2.1 utilize a representative velocity to represent the upstream boundary layer. This representative velocity must be chosen

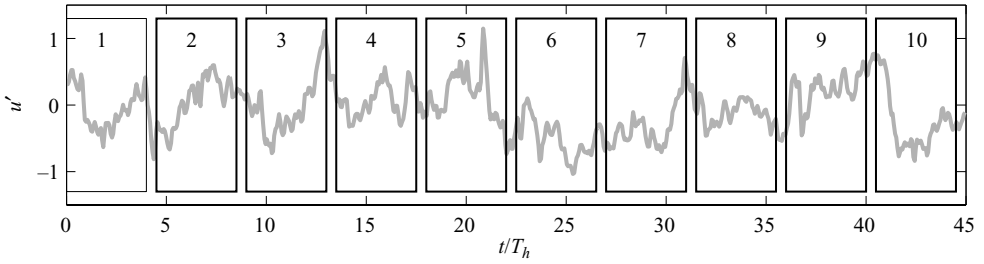

FIGURE 16. The Hot-wire data is arranged in $4T_h$ long successive blocks to simulate the adjacent placement of high-speed PIV data. The rectangles represent the field of view of PIV and a sequence that is equivalent to 10 successive PIV images is shown.

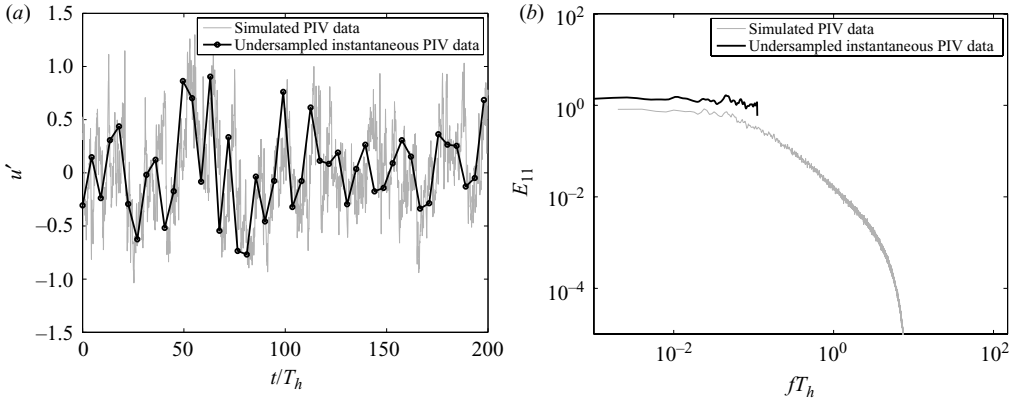

FIGURE 17. A comparison between the simulated PIV data and the instantaneous velocity at a single point. (*a*) Time trace and (*b*) Energy spectra. It must be noted that both simulated PIV data and the instantaneous velocity at a single point are obtained by modifying a well-resolved hot-wire time trace.

with some care as the velocity fluctuations in the upstream boundary layer could be aliased. Therefore, we need to systematically explore the effect of aliasing on the representative velocity. First, we will explore the effect of aliasing on a time series of an instantaneous velocity vector (i.e. we consider the representative velocity to be the velocity at a single point in the PIV image). Figure 17(*a*) shows the time trace of representative velocity based on the instantaneous value at the centre of each simulated PIV block. The corresponding energy spectrum and its comparison with the energy spectrum computed using simulated PIV data is shown in figure 17(*b*). Both figures indicate that the time series of an instantaneous velocity vector at a single point in the upstream boundary layer is prone to aliasing. Figure 17(*b*) shows that the spectrum of this representative velocity is aliased at all frequencies and does not follow the roll-off trend exhibited by the spectrum computed using the simulated PIV data. This indicates that instantaneous velocity fluctuations at a point in the upstream boundary layer cannot be used as a representative velocity.

All the analyses in § 3.2.1 use a line-averaged streamwise velocity as the representative velocity. This line-averaging process removes the small-scale fluctuations in the velocity by acting as a low-pass filter and will therefore minimize the effects of aliasing on the time trace of the representative velocity of the upstream boundary layer. The line averaging is performed over a streamwise length of 4δ (which

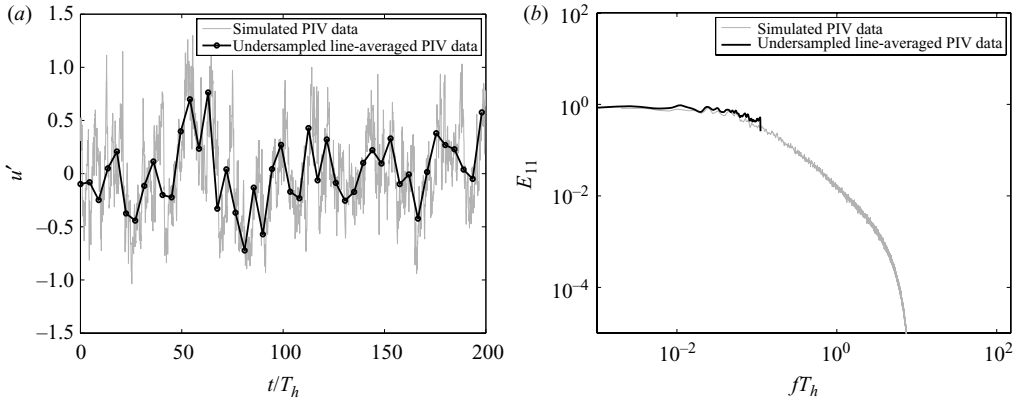

FIGURE 18. A comparison between the simulated PIV data and the under-sampled line-averaged PIV data. (*a*) Time trace and (*b*) Energy spectra. It must be noted that both simulated PIV data and the under-sampled line-averaged PIV data are obtained by modifying a well-resolved hot-wire time trace.

is equivalent to $2.7T_h$). The velocity time trace shown in figure 16 is line averaged over a length of $2.7T_h$ within each simulated PIV block and this line-averaged velocity is used as a representative velocity of that block. This is analogous to U_l in § 3.2.1 that was computed to represent the status of the upstream boundary layer. Figures 18(*a*) and 18(*b*) show the time trace of the line-averaged representative velocity and its corresponding energy spectrum, respectively. The simulated PIV data is also shown in both figures for comparison. The time trace of line-averaged velocity in figure 18(*a*) is equivalent to the time series of U_l shown in figures 7(*b*) and 8(*b*). Figure 18(*b*) indicates that aliasing effects on the line-averaged representative velocity are minimal and its effect is limited only at the highest frequency part of the spectrum. The spectrum of the line-averaged velocity follows the roll-off trend exhibited by simulated PIV data all the way to $fT_h = 0.11$ (this is the Nyquist frequency that corresponds to the acquisition rate of high-speed PIV).

Finally, the analysis in § 3.2.1 also utilizes a six-frame running-average scheme to isolate the large-scale low frequency content in the data. This scheme can also be simulated using the well-resolved hot-wire data. The running-averaged time trace is computed by applying a six-point running-average stencil on the time trace of the line-averaged velocity shown in figure 18(*a*). Figure 19(*a*) shows the time history of the under-sampled line-averaged velocity fluctuation and the time history of the under-sampled running-average filtered line-averaged velocity. The time history of the running-average filtered line-averaged velocity is analogous to the time history of running-average filtered U_l shown in figure 11(*b*). Figure 19(*a*) shows that the low-frequency content in the line-averaged velocity is retained by the running-average filtering scheme. This is further evidenced in figure 19(*b*), which shows the energy spectra of the two signals, where the running-average filter affects the frequencies greater than $fT_h = 0.01$ and does not suffer from aliasing effects at lower frequencies. The oscillations in the spectrum at higher frequencies (i.e. for $ft_h > 0.01$) are due to the transfer function of the running-average filter and not due to aliasing.

In conclusion, this appendix shows that the effect of aliasing in a under-sampled time series of a spatially well-resolved PIV measurement can be minimized by line averaging the velocities within the PIV field of view.

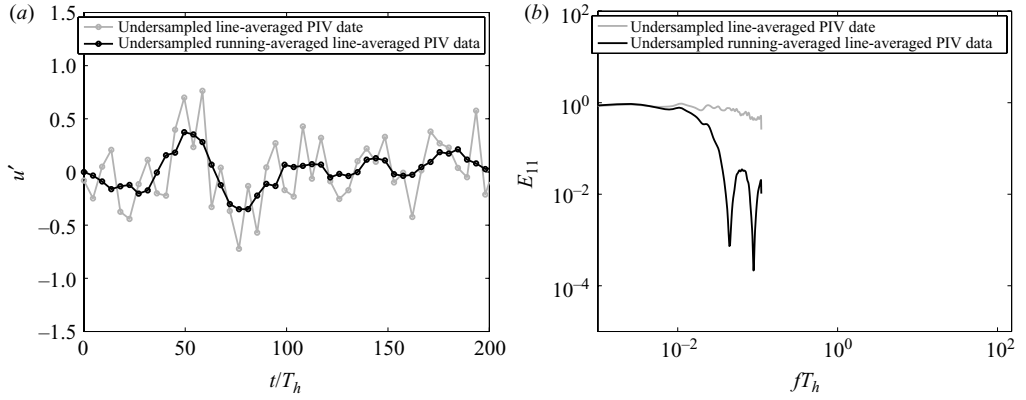

FIGURE 19. A comparison between the under-sampled line-averaged PIV data and the under-sampled running average filtered line-averaged PIV data. (*a*) Time trace and (*b*) Energy spectra. The running average is computed by applying a 6 point running average stencil to the under-sampled line-averaged time trace.

REFERENCES

BERESH, S. J., CLEMENS, N. T. & DOLLING, D. S. 2002 Relationship between upstream turbulent boundary-layer velocity fluctuations and separation shock unsteadiness. *AIAA J.* **40** (12), 2412–2422.

BUENO, P. C., GANAPATHISUBRAMANI, B., CLEMENS, N. T. & DOLLING, D. S. 2005 Cinematographic planar imaging of a Mach 2 shock wave/turbulent boundary layer interaction. *AIAA paper # 2005-0441*.

DOLLING, D. S. 2001 Fifty years of shock-wave/boundary-layer interaction research: what next? *AIAA J.* **39** (8), 1517–1531.

DUPONT, P., HADDAD, C. & DEBIEVE, J. F. 2006 Space and time organization in a shock-induced separated boundary layer. *J. Fluid Mech.* **559**, 255–277.

DUSSAUGE, J. 2001 Compressible turbulence and energetic scales: what is known from experiments in supersonic flows? *Flow Turbul. Combust.* **66**, 373–391.

DUSSAUGE, J. P., DUPONT, P. & DEBIEVE, J. F. 2006 Unsteadiness in shock wave boundary layer interactions with separation. *Aerosp. Sci. Technol.* **10**, 85–91.

GANAPATHISUBRAMANI, B. 2007 Statistical properties of streamwise velocity in a supersonic turbulent boundary layer. *Phys. Fluids* **19**, 098108.

GANAPATHISUBRAMANI, B., CLEMENS, N. T. & DOLLING, D. S. 2006 Large scale motions in a supersonic turbulent boundary layer. *J. Fluid Mech.* **556**, 271–282.

GANAPATHISUBRAMANI, B., CLEMENS, N. T. & DOLLING, D. S. 2007 Effects of upstream boundary layer on the unsteadiness of shock induced separation. *J. Fluid Mech.* **585**, 369–394.

HOU, Y. X. 2003 Particle image velocimetry study of shock induced turbulent boundary layer separation. PhD thesis, Department of Aerospace Engineering and Engineering Mechanics, The University of Texas at Austin, TX.

HOU, Y. X., CLEMENS, N. T. & DOLLING, D. S. 2003 Wide-field PIV study of shock-induced turbulent boundary layer separation. In 41*st Aerospace Sciences Meeting and Exhibit, 6–9 January 2003*, Reno, NV.

HUMBLE, R. A., ELSINGA, G. E., SCARANO, F. & VAN OUDHEUSDEN, B. W. 2009 Three-dimensional instantaneous structure of a shock wave/turbulent boundary layer interaction. *J. Fluid Mech.* **622**, 33–62.

HUTCHINS, N. & MARUSIC, I. 2007 Evidence of very long meandering features in the logarithmic region of turbulent boundary layers. *J. Fluid Mech.* **579**, 1–28.

MÜLLER, J., MÜMMLER, R. & STAUDACHER, W. 2001 Comparison of some measurement techniques for shock-induced boundary layer separation. *Aerosp. Sci. Technol.* **5**, 383–395.

RINGUETTE, M. J., WU, M. & MARTIN, M. P. 2008 Coherent structures in direct numerical simulation of turbulent boundary layers at Mach 3. *J. Fluid Mech.* **594**, 59–69.

Samimy, M., Arnette, S. A. & Elliot, G. S. 1994 Streamwise structures in a supersonic turbulent boundary layer. *Phys. Fluids* **6** (3), 1081–1083.

Settles, G. S., Vas, I. E. & Bogdonoff, S. M. 1976 Details of a shock-separated turbulent boundary layer at a compression corner. *AIAA J.* **14** (12), 1709–1715.

Smits, A. J. & Dussauge, J. P. 1996 *Turbulent Shear Layers in Supersonic Flow*. American Institute of Physics Press.

Spencer, A. & Hollis, D. 2005 Correcting for subgrid filtering effects in particle image velocimetry data. *Meas. Sci. Technol.* **40** (11), 2323–2335.

Tomkins, C. D. & Adrian, R. J. 2003 Spanwise structure and scale growth in turbulent boundary layers. *J. Fluid Mech.* **490**, 37–74.

Weiss, J. & Chokani, N. 2007 Effect of free stream noise on shock-wave/turbulent boundary layer interactions. *AIAA J.* **45** (9), 2352–2355.

Wu, M. & Martin, M. P. 2008 Analysis of shock motion in shockwave/turbulent boundary layer interaction using direct numerical simulation data. *J. Fluid Mech.* **594**, 71–83.